Supplementary materials: "Great Himalayan earthquakes and the Tibetan Plateau"

Nicole Feldl and Roger Bilham

We provide details of GPS data acquisition and analysis from 1991-2004, plus information on modeling these GPS data first as slip on a planar fault with uniform slip and dip beneath southern Tibet, and then as slip on a geometrically complex surface driven from >500 km to the north. We describe typical 3d-def boundary element input files of the form we used in our calculations. These files are named *b150section* and *m300map*. A version of the 3d deformation program[22-24] compiled in Fortran 91 is provided as an additional supplement (*3ddef.tar*).

Data from Nepal

Since first submission of this article a rigorous analysis of GPS and DORIS points in Nepal has been published[1]. We here report our analysis of a subset of those GPS points and additional points in eastern and central Nepal that were measured in 2003-2004 and were not included in that analysis. Inasmuch as our solutions agree within the respective uncertainties, our data are presented to complement this previous analysis and to provide a starting point for the models we later discuss. The most northerly of these sixteen points are JOMS in the Kali Gandaki valley and KPFB in the Khumbu valley, a few kilometers west of Everest (see Figure 1 in main text). Some of these points were first measured in 1991, although pre-1992 data were discarded due to reference frame errors induced by the absence of a global GPS tracking network and unavailability of precise satellite orbits. Measurements were made in campaign style surveys, supplemented by brief segments of continuous tracking at four sites. The 13 year span of raw GPS data (Table 1) were analyzed using Bernese 4.2 software[2] with continuous station data from the IGS network to generate a global solution in ITRF2000: 36-37 IGS stations with global coverage were included in the 1998-2004 solution, 31-32 for 1996-1997, 27 for 1995, and 12 for 1992. Precise CODE final satellite orbits and antenna phase-center offsets were included in the analysis. Receiver clock errors and cycle slips were removed prior to processing, and ambiguities were resolved for each baseline using a quasi-ionosphere-free strategy. Troposphere parameters for each site were estimated every two hours. Surface velocities were calculated from the weighted combination of daily free-network coordinate solutions. The free solution was computed by minimizing the coordinate transformation of the IGS00 station coordinates, a precise subset of the ITRF2000 network, onto their known coordinates. The resulting solution includes coordinate and velocity estimates for all the stations and is consistent with the ITRF2000 reference frame. The resulting a posteriori sigma of unit weight for the combination was 0.0015.

The effects of angular rotation [3,4] between India and Asia were suppressed by determining relative velocities within the study area; between BIRP and points in eastern Nepal, and between BHAI and points in central Nepal, assuming the arc-normal velocities of BIRP and BHAI are identical. Resulting angular errors are <1° over the

scale of the network. Velocities from points in southern Tibet were included to constrain velocities immediately north of Nepal, and the data were resolved into their arc-normal component, N5ºE and N18ºE for eastern and central Nepal respectively. The relative velocity of BIRP/BHAI was then inferred from the synthetic velocity curve generated by the planar elastic dislocation model that best fits the observations. Hence in Figure 2, the velocity of BIRP/BHAI relative to fixed India is ~1.7 mm/yr.

Standard deviations in ITRF2000 were propagated into the new local reference frame. For the east (and north) components of velocity, the 1σ uncertainty in the local reference frame is given for each station by

$$\sigma_E = \sqrt{\sigma_e^{\,2} + \sigma_{fix}^{\,2}} \quad (1)$$

where σ_e is the standard deviation of the velocity in ITRF2000 and σ_{fix} is the standard deviation of the fixed station velocity (BHAI or BIRP) in ITRF2000. The standard deviation of the arc-normal velocity is given by

$$\sigma_{horz} = \sqrt{\frac{\sigma_E^{\,2}\sigma_N^{\,2}}{\sigma_N^{\,2}\cos^2\theta + \sigma_E^{\,2}\sin^2\theta}} \quad (2)$$

where σ_E is the standard deviation of the east velocity, σ_N is the standard deviation of the north velocity, and θ is the bearing of the convergence vector, counterclockwise from east.

GPS data north of the Himalaya

Starting some 50 km north of the Himalaya a strain rate of 17-18 μm/yr is established[5,6] that extends throughout much of Tibet. In our study area (83-90°E, 26-33°N shown in Figure 1 of main article) we include a re-analysis of a subset of the Chen et al.(2004)[7] velocities and find a strain rate at N10E of 17.9±1 x10^{-8}/yr (Figure 1). The recent compilation by Bettinelli et al.[1] includes results from Chen et al. in southern Tibet which they convert to an ITRF2000 frame of reference. In this article we also include the results of Zhang et al. and Chen et al. up to 600 km from the frontal thrusts suitably adjusted for frames of reference and projected onto a N10E section.

We combined the ITRF2000 data sets of this study and Zhang et al. into an India-fixed frame. Velocities from this study were calculated relative to BHAI in central Nepal and BIRP in eastern Nepal. The Zhang et al. velocities were calculated relative to the Zhang velocity for BHAI. Uncertainties were propagated from the absolute velocity uncertainties of each study, according to Equation 1 above.

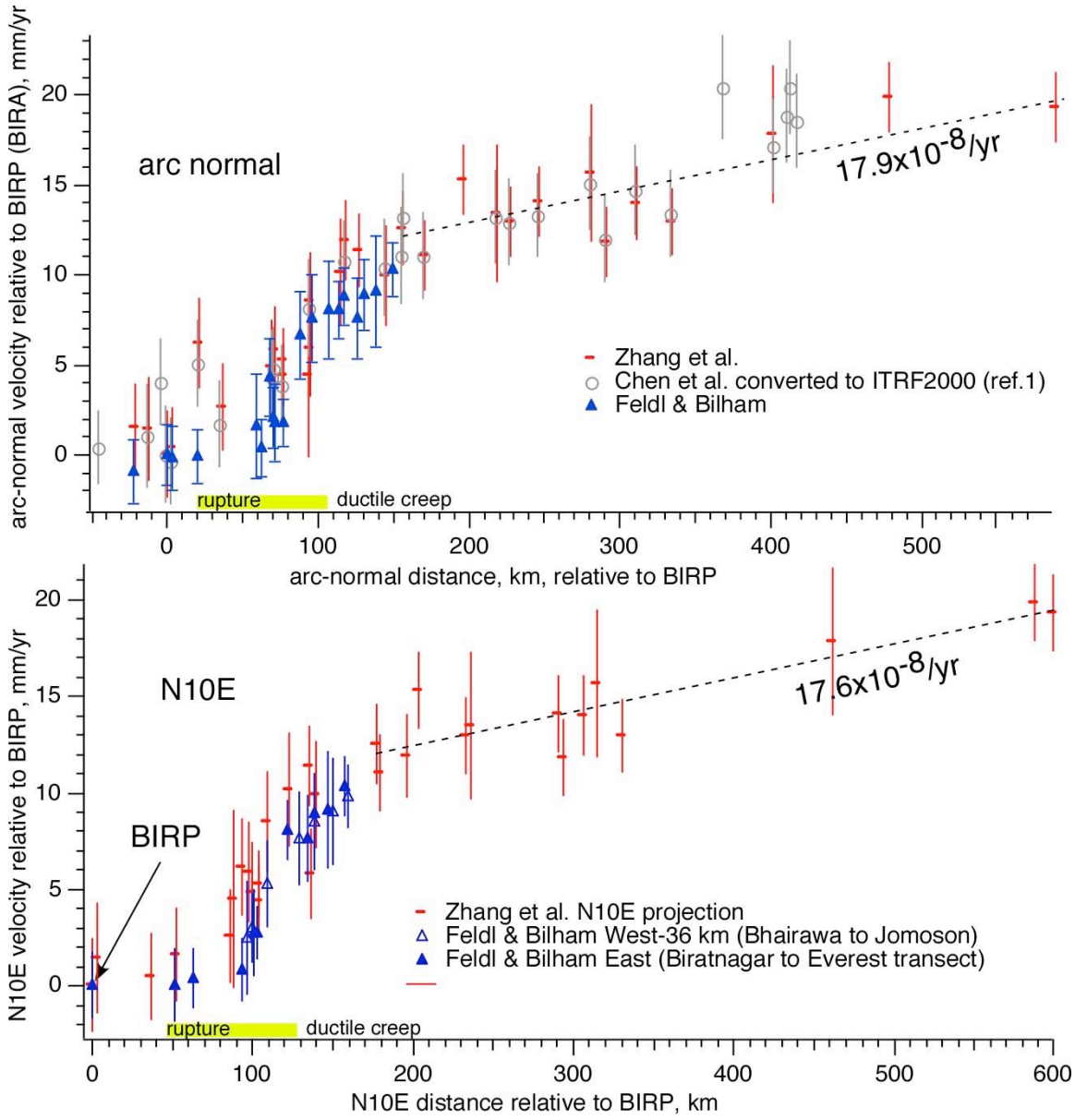

Figure 1 Arc-normal and N10E velocities relative to Biratnagar (BIRP/BIRA). The velocity of Biratnagar is approximately 1±2 mm/yr relative to the Indian Plate[1]. We use the ITRF 1997 points of Chen et al (2004)[7] converted to ITRF2000[1] The frontal thrusts emerge at 20-30 km on the distance axis and the mean 3.5 km contour, the zero datum of all models in this article, crosses near Lukla at 120 km. The distance between these two points is the approximate width of rupture of Himalayan earthquakes (here in yellow; Bettinelli et al.[1] propose a width of 115 km). We have offset the western Nepal points by 36 km in the lower plot to adjust for the relative position of the locking line caused by the curvature of the arc.

Planar Elastic Models

We initially modeled the southernmost 100 km of the observed Himalayan velocity field, as have previous investigators[8], as the product of uniform slip on one or more planar faults embedded in an elastic half-space. For this planar elastic dislocation model, we

used the Nepal velocities calculated in this study and the velocities of RONG and TING (See figure 1 of published article) from Tibet[5]. A 2-D single fault approximation[9] provides an adequate fit to the somewhat scattered data as long as arc curvature is negligible over the length of the model, although a physically more satisfying fit can be obtained by incorporating additional structural and geometrical data and solving for vertical deformation simultaneously[1]. In eastern Nepal (86.5°-88.5°E) we adopted a strike of N95ºE and in central Nepal (82.5º-86.5º) N108ºE, parallel to trends of mapped microseismicity [12,13]. Although separate elastic models for central and eastern Nepal provide a marginally better fit to the observations than the ensemble analysis, the locking line for the entire data set better approximates the locus of the microseismicity peak with which it has been associated [10,12] (Table 2).We conclude from Figures 2 & 3 that the best fitting planar dislocation has a uniform velocity of 17±1 mm/yr dipping 9° arc normal.

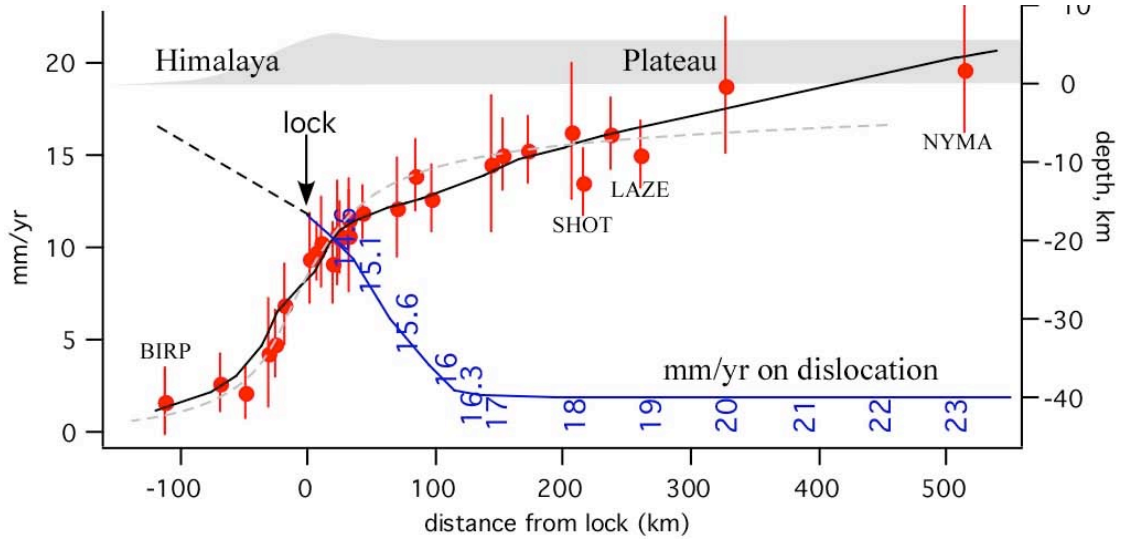

Figure 2. Combined GPS data (one standard deviation) from this study and Zhang et al. and synthetic fits for 17 mm/yr uniform slip on a 6° planar dislocation (dashed line), and for imposed northward increasing slip on a geometric surface beneath southern Tibet defined by receiver function analysis[18]. The surface velocity field (top right and cross-section below) is emulated by a series of contiguous dislocations increasing in slip velocity northwards at 17 µm/km/yr, starting from a tip velocity near the locking line of 13.5±3 mm/yr (one sigma). The applied displacement on the geometrical surface shown here is thus a forward model inferred and modified from the observed surface velocity field (Figure 1), rather than calculated from an elastic model as we do later (see Figure 2 of published article). We show it in this figure merely to demonstrate that it leads to a quite reasonable fit to the data.

We qualify this statement by pointing out that the small uncertainty and the derived rate applies only to the subset of points that we selected for our analysis. Had additional data been incorporated northward into Tibet, the best fitting velocity and its uncertainty would increase. This results from the incorporation of points that define the NNE strain contraction of Tibet. The Himalayan collision does not occur between two rigid plates[10]. The difficulty in deciding where to cut off the data in the north is avoided in later elastic models that emulate Tibet's NNE directed contraction and thereby fit these northern points. The most important finding from these models is the recognition that the selection of increasingly more northerly GPS points in the planar model raises the

inferred slip velocity, a reason why we should not expect many of the reported velocities in the past several years to have converged on a single precise "collision velocity" [1,11-16] despite the accumulation of data that should reduce velocity uncertainties with time.

It is well known that the singularity associated with the termination of uniform slip on a planar dislocation is avoided on a real fault because slip tapers to zero over a finite distance near the tip of the fault. An analytical form of this tapered-slip is available in the form of an elliptical decay in slip towards the locked tip, however, vertical uplift is much reduced in such models, so much so that they have found no application in the Himalaya. We found, however, that this elliptically tapered slip when applied to the sigmoidally shaped interface of the descending Indian plate as quantified from a receiver-function analysis across the Himalaya[18] yields a substantially better fit to both vertical and horizontal data. In Figure 2 we show both the planar fit and the fit from a forward model derived by trial and error. The starting point for deriving slip imposed on each planar segment in the curved interface model was derived from the observed surface velocity field. The curved interface model was fit to data combined from this study and from Zhang et al., (2004)[6] as compared to the planar dislocation model, which was fit to the smaller subset of data from this study and the velocities of RONG and TING[5] (for locations see Figure 1 of main published article and for discussion see Chen et al., 2004 [7].

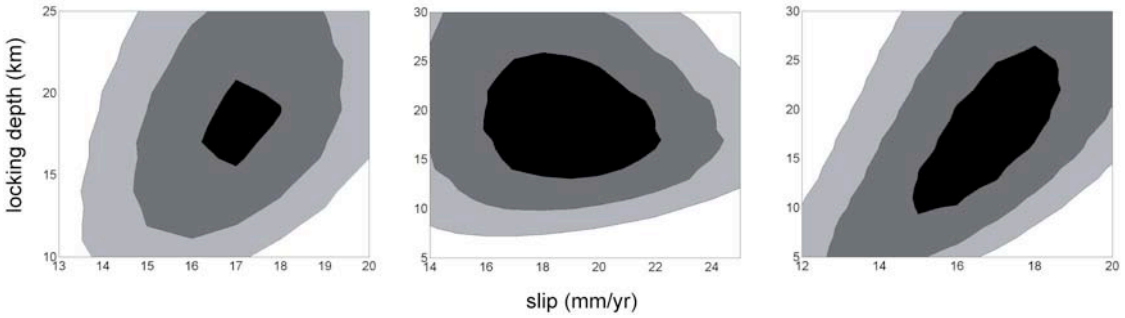

Figure 3 Trade-off between locking depth and slip parameters in planar dislocation modeling (Figure 2), for the combined data, central, and eastern Nepal (left to right). The contours mark the 1s, 2s, and 3s confidence limits. The best fitting dislocation for the combined data yields a slip of 17±1 mm/yr with a locking depth of 18 km.

Tapered slip can also be emulated from a consideration of the frictional properties of the sub-Himalayan interface and its surrounding rheology[10,19-21]. However, the effects of friction are important only if the viscous component of slip on the interface has a long time constant compared to the interseismic duration of the earthquake cycle. During the period of post-seismic adjustment the rheology of the interface moderates slip rates, but if the time constant of viscous drag is less than a decade the interface behaves as though it were frictionless during the interseismic period. With this caveat, we conclude that the geometry of the interface is more important than its rheology. We calculate minimum-coseismic and maximum post-seismic slip in models.

We subsequently abandoned modeling estimates of surface velocity fields produced by complex subsurface geometries where a pre-conceived distribution of slip is applied to

subsurface elements, in favor of models in which this slip distribution is calculated from the geometry and stresses of the collision. This approach, which forms the main thrust of our article, emulates the collision zone as a series of boundary elements driven from the north.

Boundary element models

We use the subsurface geometry of the Himalaya [17] as a starting point and defined a series of segment boundaries to drive and respond to plateau convergence (Figure 4 &5). We initially ran a series of models that started 1000 km north of the Himalaya and treated the Himalaya at depth as a 3600-long "cylindrical" extruded sigmoidal interface to avoid edge effects. We divided this surface into a sufficient number of segments so as to be able to drive the shortest earthquake rupture of interest - 50 km along strike (Figure 5). We found the models not particular sensitive to the segment density and although we were able to emulate GPS convergence rates througout Tibet, to economize on computing time we used a coarser grid for most of the models presented. Thus our initial models used >1800 elements (requiring 4 hour computing runs and much increased allocations for array space in 3d-def) and later ones fewer than 750. We found that the model results were also not particularly sensitive to the distance north of the northern boundary driving element so we eventually, and with encouragement from reviewer Jeff Freymueller, opted to drive the system from 594 km north of the Indian plate (≈500 km north of the Himalaya). This shorter boundary condition avoids the adoption and interpolation of GPS data from further north into Tibet which is unavailable directly north of our region of interest. It also corresponds approximately with the Jiali seismic zone, a prominent tectonic boundary in central Tibet.

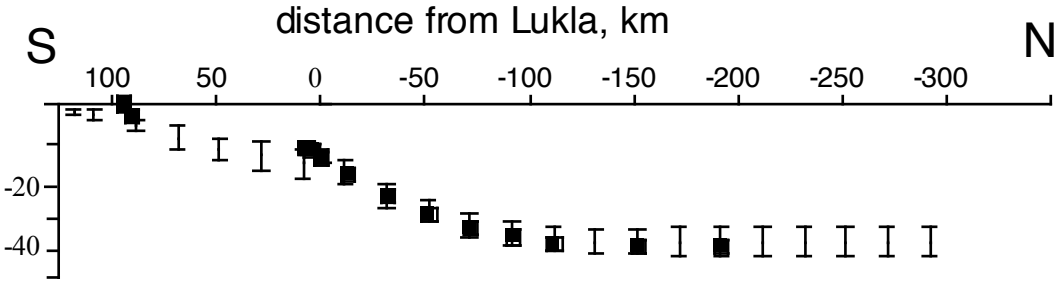

Figure 4 Subsurface geometry of the India/Tibetan plateau interface beneath the Himalaya and southern Tibet. The error bars show the range of depths estimated from [17] and the square markers indicate the preferred geometry required to obtain the best fitting models indicated in Fig 2 of the main article. We found the creeping interface to approach 15 km of the surface and to extend 7.5 km south of the locking line of best fitting planar models.

Having modified the subsurface geometry to one that best emulates the observed surface velocity field (Figure 5a) we record the resulting elemental slip velocity. From these velocities we calculate the displacements on these sub-surface segments corresponding to 1000 years of present-day slip, and for a second boundary-element model (Figure 5b) in which the area of freely slipping boundary elements is extended southwards, as occurs rapidly during an earthquake. We choose a 6-12° NNE dipping planar surface for this

extended rupture, with or without a ramp dipping more steeply to the surface near the Main Boundary faults of the Himalaya. The extended slip zone changes the location of the southernmost locked line in the case of short (<80 km) blind reverse fault, and makes it emerge at the surface in the case of a long (>90km) rupture.

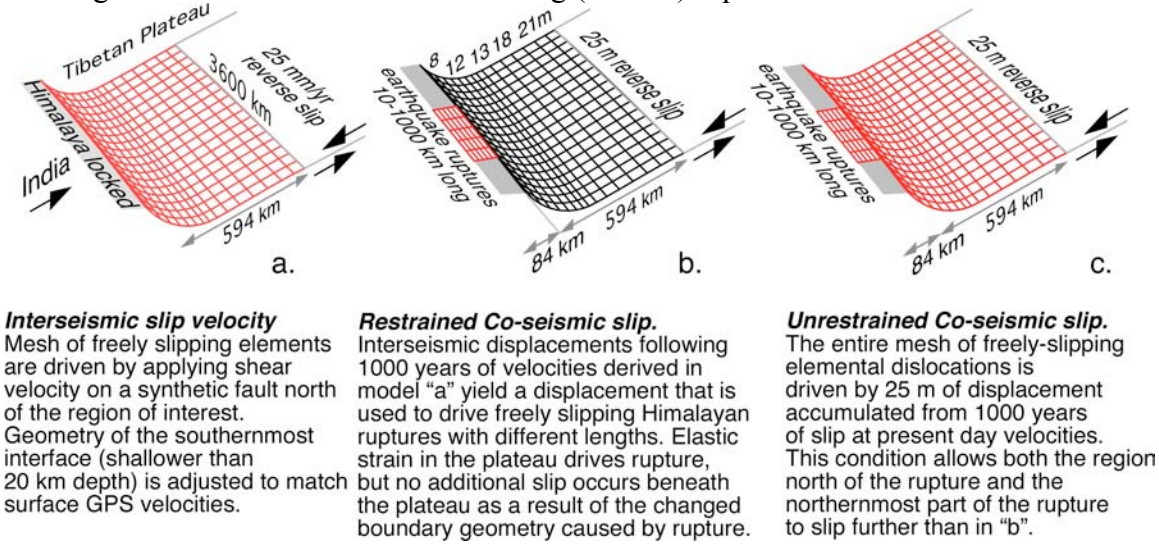

Figure 5. The mesh and conditions for the three boundary element models used. All are driven by a horizontal thrust fault 2000 km wide starting 594 km north of India, and an imposed contraction rate of 4.9×10^{-8} strain/year. Red elements slip freely. Black elements have specified slip. **a.** Interseismic surface velocities are emulated by adjusting the geometry of the southernmost elements as shown in Figure 4. **b.** Shows the restrained slip condition appropriate for instantaneous pre-seismic displacements driving a frictionless dislocation beneath the Himalaya. **c.** Slip of the rupture changes the southernmost boundary condition for the entire model. This unrestrained condition represents the fully relaxed afterslip condition.

The interseismic slip distribution throughout the plateau (calculated above) is modified by this extended rupture zone and responds by increasing displacements especially close to the former locked tip of the ductile creeping zone (Figure 5c). Not all of this displacement will be expressed at the time of the earthquake since it occurs in the zone of ductile creep. Thus much of the resulting redistribution of slip on the interface caused by very long ruptures is presumably manifest in afterslip[21]. The instantaneous (5b) and afterslip (5c) synthetic slip calculated for Himalayan ruptures in this way offer minimum and maximum estimates for moment magnitude respectively. It is probable that moment release immediately north of long ruptures will be partly seismic, permitting coseismic magnitudes somewhere between the two extremes to occur on the basal thrust fault beneath the Himalaya. The synthetic slip distribution on renstrained planar rupture zones shows maximum slip near their northern edges. The dynamics of slip near the free surface, however, will permit these large coseismic slips (≥20 m) to be manifest locally on the MBT as surface rupture.

Elastic and inelastic strain and east-west extension

The fraction of the total strain released by earthquakes varies with the length of the rupture. We note in our models, however, that even for the largest earthquakes as much

as 80% of the strain north of the Himalaya remains untapped by coseismic slip (Figures 6 and 7). This residual strain remains to drive inelastic N/S convergence and east-west extension of Tibet. Although it is possible to quantify the proportion of inelastic and elastic strain in the earthquake cycle for single events, and is in fact dominated by the largest earthquakes, the actual apportionment in practice depends on the cumulative effects of many earthquake cycles involving a range of different length ruptures, and is beyond the scope of the present article.

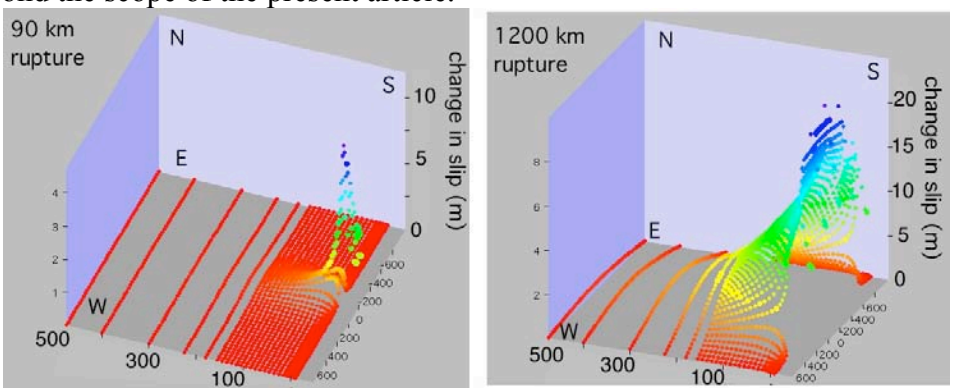

Figure 6. An example of boundary element changes in displacement for 90-km-long and 1200-km-long ruptures for unrestrained slip beneath the Tibetan Plateau extending south into each rupture. Each colored dot is a freely slipping element. We show the change of slip on all elements accompanying an earthquake that extends the southern locking line southward, as occurs in an earthquake. Where the rupture is short, earthquake slip is low, and displacements beneath Tibet are relatively modest. Where the rupture is long, rupture slip approaches the full applied preseismic displacement, and occurs over a wide region beneath Tibet although not all of it can be released coseismically. East-west and north-south distances are in km, whereas the z axis is in m, color coded to emphasize slip .

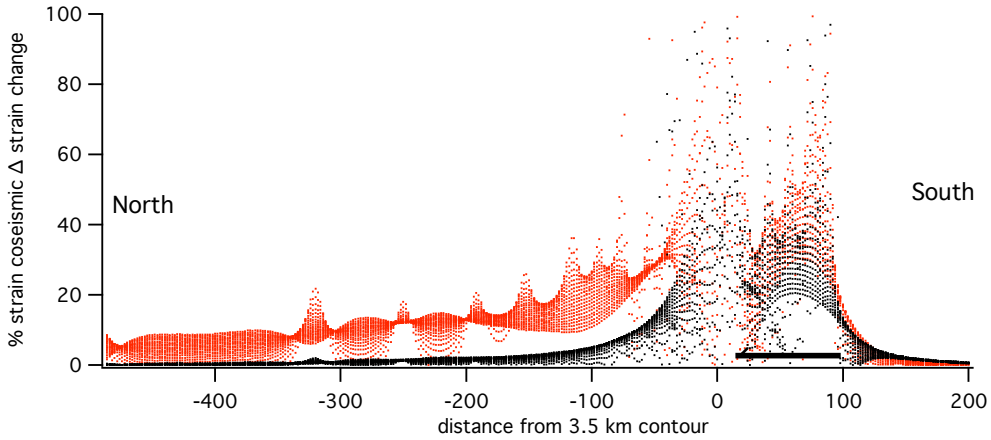

Figure 7 Percentage dilatational strain change throughout the uppermost 40 km of the plateau accompanying 100-km-long (black) and 600-km-long (red) ruptures. Even for a 600-km-long rupture, cyclic strain changes in the plateau are less than 20%, leaving the remaining 80% to drive anelastic deformation in the plateau. The cusps are artifacts of segment boundaries and their effects are much attenuated in models with smaller segments. The upper edge of each envelope in each case is the region north of each rupture, and the lower edge of the envelope are regions far E & NE and W & NW of each rupture. Synthetic earthquake ruptures propagate from -7.5 km to 94 km south of the 3.5 km contour (black bar right).

In Figure 5 in the main article we provide cross-sections and map views of the strain changes associated with 100 km and 600 km long ruptures to illustrate the strain changes that accompany earthquakes with different rupture lengths. Note that strain is depleted more for the case of the 600 km long rupture, and that this is evident more clearly in the section than in the map view, which shows only surface strain.

In these models the maximum cyclic *east -west* strains and displacements occur in the range 50-100 km north of the Himalaya. These result from Poissons' ratio effects that grow during the interseismic period and are released by great earthquakes in the Himalaya. We note they occur along that part of the southern plateau most densely populated by tensile grabens and half grabens. Given this association it would not be unexpected if seismicity in the grabens were linked to strain accumulation and release associated with great earthquakes in the Himalaya.

Table 1 GPS station coordinates nd ITRF2000 velocities from this study for east and north components with 1σ uncertainty. The number of observing sessions are indicated in the ten columns right. Data from 1992 were collected in 8-hour sessions; 24-hour sessions were conducted in 1995-2004.

Station	*Lat.ºN*	*Long.ºE*	*East mm/yr*	*N. mm/yr*	*92*	*95*	*96*	*97*	*98*	*99*	*00*	*01*	*03*	*04*
JOMS	28.780	83.717	33.82±1.08	24.31±0.98	3	9			4				4	
P109	28.199	83.981	33.11±1.27	31.33±1.23					12				9	
BENI	28.347	83.561	35.93±1.86	28.57±1.80					9				5	
GANS	28.599	83.642	35.78±2.24	25.25±2.12					4				5	
JALT	28.507	83.658	34.98±2.17	26.34±2.06					5				6	
KUSU	28.210	83.677	35.25±2.53	31.45±2.61					2				4	
TUKO	28.709	83.644	33.65±2.38	25.13±2.46					4				4	
KPFB	27.993	86.827	37.48±0.94	22.21±0.95			10	4	3	3			27	1
LUKL	27.686	86.726	38.55±1.18	24.25±1.04		4	1				4		5	3
NAMC	27.802	86.715	39.61±2.46	24.58±1.86			20	13			6			
PHER	27.894	86.822	40.08±2.99	22.98±2.82			2	4			4		4	5
TANG	27.835	86.764	38.29±1.64	23.47±1.57			5				7		2	3
BHAI	27.507	83.417	37.85±1.67	33.52±1.34	3									3
TANS	27.873	83.553	35.02±0.99	33.18±0.93	3									3
BIRP	26.483	87.267	37.90±1.30	32.57±1.20			10	9	19	26				3
HILE	27.049	87.326	36.57±1.06	32.40±0.97		5						5		2
NAGA	27.692	85.521	36.06±0.43	31.09±0.39	9	11	33	14	13	11	12	10	12	
SIMA	27.162	84.981	41.49±1.46	32.11±1.27	3	4	11	17	16	17	5			
AIRP	27.697	85.357	30.72±1.82	32.04±1.78		3			5					

Table 2 Reported Himalayan slip rates based on planar dislocation estimates for this study[25].

Interval	Slip rate (mm/yr)	Locking depth (km)	Dip (º)	Location	c^2
1992-2004	17±2	18	9	eastern Nepal	1.053
	19±3	18	6	central Nepal	0.276
	17±1	18	9	combined	1.633

Input files section400 and 300map, and executable program.

Typical 3d-def input text files[22-24] used in this study are provided as dowloadable ascii files. *Section400* and *300map* calculate unrestrained slip on 400-km-long and 300-km-long ruptures respectively. They can be used directly as input to 3d-def .

The input file *300map* is for a 300-km-long unrestrained rupture with a total of 29 planes each divided into 50 segments along strike, driven by a reverse fault 1000 km north of the Himalaya. The first two planes are a rupture fronting the Himalaya divided into five segments along-strike and five elements down-dip, the first being a steep ramp and the second a gently dipping decollement. It outputs a map view of the surface strain (suffix .m300) and a segment displacement listing in a north-south line through the center of the rupture. Columns 2 and 3 after the line that starts "for each plane" indicate the start points (distance and depth) of each segment, and columns 5 and 9 indicate the length and dip respectively. The along-strike length of the interseismic driving condition is 3600 km and in this model each segment width is 56.25 km. All elements are freely-slipping (code 12) except the most northerly plane and last listed plane segment 30 (code 10) which drives the system at 35 mm/year, or in the case of coseismic rupture with an imposed displacement of 35 m. The first two planes specified are the Himalayan rupture, the first plane representing a 45° north-dipping 5.7-km-long ramp-thrust that cuts the surface . If these planes are removed and the number of planes reduced from 17 to 15 in line 2, the file can be used to calculate pre-seismic displacements or interseismic velocities. Strain and displacement changes accompanying rupture can then be obtained by subtracting the two output matrices. This file executes in about 4 hours on a 1 GHz Apple Powerbook-Pro running in UNIX. For experimental purposes to speed up the computation, the size of each section or map can be decimated by dividing the numbers in the last line of code by ten.

The second file, *section400,* differs in its length (1700 km), width (it is driven from 500 km north of the Himalaya, and the output section with suffix .i400 it calculates instead of map view. It also has fewer segments to speed computation. Sixty four along-strike segments are placed beneath the southern plateau, reducing to thirty-two 72 km north of the locking line. As before the rupture consists of two planes each with 25 segments. The system here is driven at 25 mm/year. Both files output shear and dilatational strain, displacement or velocity, and displacement of velocity on the subsurface segments.

3ddef.tar

The 3ddef Fortran code downloaded from the CERI web site[23] must be modified to process the large matrices inverted in the present analysis. The code provided (256kb) has been modified appropriately and can invert the large arrays used to examine slip on hundreds of freely-slipping elements in this article. We are indebted to Walter Szeliga, University of Colorado, for these modifications. A compiled Fortran 91 version of this code that runs in the UNIX terminal mode of Apple computers can be downloaded as a .tar file. Place the input files *section400* or *300map* in the folder 3ddef once it has been

de-compressed. To run the program 3ddef on the desktop screen from "Terminal", change to the directory to 3ddef [cd desktop/3ddef] then type ./3d and enter the appropriately named input file when prompted. The program will run in the background, but will be faster if no other tasks are running.

—

References

1. Bettinelli, P., J.P. Avouac, M. Flouzat, F. Jouanne, L. Bollinger, P. Willis, and G.R. Chitraker, Plate motion of India and interseismic strain in the Nepal Himalaya from GPS and DORIS measurements, Journal of Geodesy, doi: 10.1007//s00190-006-0030-3, 2006.
2. Beutler, G. et al. (eds. Hugentobler, U., Schaer, S. & Fridez, P.) (Astronomical Institute, University of Berne, Switzerland, 2001).
3. Gordon, R. G., Argus, D. F. & Heflin, M. B. Revised estimate of the angular velocity of India relative to Eurasia. *EOS, Transactions of the American Geophysical Union* **80**, F273 (1999).
4. Sella, G. F., Dixon, T. H. & Mao, A. REVEL: A model for Recent plate velocities from space geodesy. *Journal of Geophysical Research* **107** (2002).
5. Wang, Q. et al. Present-Day Crustal Deformation in China Constrained by Global Positioning System Measurements. *Science* **294**, 574-577 (2001).
6. Zhang, Pei-Zhen, Shen, Zhengkang, Wang, Min, Gan, Weijun, Bürgmann, R, Molnar, P, Wang, Qi, Niu, Zhijun, Sun, Jianzhong, Wu, Jianchun, Hanrong, Sun, Xinzhao, You, Continuous deformation of the Tibetan Plateau from global positioning system data**,** Geology 2004 32: 809-812
7. Chen, Q., J. T. Freymueller, Z. Yang, C. Xu, W. Jiang, Q. Wang, and J. Liu (2004), Spatially variable extension in southern Tibet based on GPS measurements, J. Geophys. Res., 109, B09401, doi:10.1029/2002JB002350.
8 Vergne J., R. Cattin and J.P. Avouac, On the use of dislocations to model interseismic strain and stress build-up at intracontinental thrust faults, *Geophys. J. Int.,*147, 155-162, 2001.
9. Savage, J. C. A dislocation model of strain accumulation and release at a subduction zone. *Journal of Geophysical Research* **88**, 4984-4996 (1983).
10. Avouac, J. P. Mountain Building, Erosion, and the Seismic Cycle in the Nepal Himalaya. *Advances in Geophysics* **46**, 1-80 (2003).
11. Jouanne, F. et al. Current shortening across the Himalayas of Nepal. *Geophysical Journal International* **157**, 1-14 (2004).
12. Pandey, M. R., Tandukar, R. P., Avouac, J. P., Vergne, J. & Heritier, T. Seismotectonics of the Nepal Himalaya from a local seismic network. *Journal of Asian Earth Sciences* **17**, 703-712 (1999).
13. Bilham, R., Larson, K., Freymueller, J. & Project Idylhim members. GPS measurements of present-day convergence across the Nepal Himalaya. *Nature* **386**, 61-64 (1997).
14. Burgmann, R., Larson, K. & Bilham, R. Model Inversion of GPS and Leveling Measurements Across the Himalaya: Implications for Earthquake Hazards and Future Geodetic Networks. *Himalayan Geology* **20**, 59-72 (1999).

15. Larson, K., Burgmann, R., Bilham, R. & Freymueller, J. Kinematics of the India-Eurasia collision zone from GPS measurements. *Journal of Geophysical Research* **104**, 1077-1093 (1999).
16. Jade, S. et al. GPS measurements from the Ladakh Himalaya, India: Preliminary tests of plate-like or continuous deformation in Tibet. *Geological Society of America Bulletin* **116**, 1385-1391 (2004).
17. Banerjee, P. & Burgmann, R. Convergence across the northwest Himalaya from GPS measurements. *Geophysical Research Letters* **29** (2002).
18. Schulte-Pelkum, V. et al. Imaging the Indian Subcontinent beneath the Himalaya. *Nature* (2005).
19 Cattin, R. & Avouac, J. P. Modeling mountain building and the seismic cycle in the Himalaya of Nepal. *Journal of Geophysical Research* **105**, 13389-13407 (2000).
20. Perfettini, H. & Avouac, J. P. Postseismic relaxation driven by brittle creep: A possible mechanism to reconcile geodetic measurements and the decay rate of aftershocks, application to the Chi-Chi earthquake, Taiwan. *Journal of Geophysical Research* **109** (2004).
21. Perfettini, H. & Avouac, J. P. Stress transfer and strain rate variations during the seismic cycle. *Journal of Geophysical Research* **109** (2004).
22. Gomberg, J. & Ellis, M. Topography and tectonics of the central New Madrid seismic zone: Results of numerical experiments using a three-dimensional boundary-element program. *Journal of Geophysical Research* **99**, 20299-20310 (1994).
23. http://www.ceri.memphis.edu/people/ellis/3ddef/gettingstuff.htm
24. http://www.ceri.memphis.edu/people/ellis/3ddef/index.html
25 http://cires.colorado.edu/~feldl/feldl_thesis.pdf